

RESEARCH ARTICLE | JULY 20 2018

Effects of Reynolds number and thickness on an undulatory self-propelled foil

Dong Zhang; Guang Pan ; Liming Chao; Ya Zhang



Physics of Fluids 30, 071902 (2018)

<https://doi.org/10.1063/1.5034439>



View
Online



Export
Citation

Articles You May Be Interested In

Scaling law of fish undulatory propulsion

Physics of Fluids (June 2021)

Investigation on the performance of a torque-driven undulatory swimmer with distributed flexibility

Physics of Fluids (February 2024)

Preliminary investigation of yaw stability in undulatory fish propulsion using stability derivatives

Physics of Fluids (July 2024)



Physics of Fluids

Special Topics Open
for Submissions

[Learn More](#)

Effects of Reynolds number and thickness on an undulatory self-propelled foil

Dong Zhang, Guang Pan,^{a)} Liming Chao, and Ya Zhang

School of Marine Science and Technology, Northwestern Polytechnical University, Xi'an 710072, China and Key Laboratory for Unmanned Underwater Vehicle, Northwestern Polytechnical University, Xi'an 710072, China

(Received 11 April 2018; accepted 25 June 2018; published online 20 July 2018)

The effects of the Reynolds number (Re) and thickness on an undulatory self-propelled foil were numerically investigated using the immersed boundary method. Re varied from 50 to 2×10^5 , which encompasses the viscous, intermediate, and inertial regimes using a NACA 0012 airfoil. An investigation of the thickness was performed on NACA airfoils with maximum thicknesses of $0.04 \sim 0.24$ at two Re values (5×10^4 and 500). The results indicated that the foil can achieve a higher forward velocity, perform less work, and exhibit a higher propulsive efficiency with increasing Re . However, the effect of Re is asymptotic beyond 5×10^4 . Four types of vortex structures exist, and the transition from one regime to another is closely related to hydrodynamic changes. In the thickness study, thinner foils outperformed thicker foils in terms of the forward velocity and input power at both Re values. However, the efficiency related to the conversion of input power into kinetic energy for NACA 0004 was the lowest. An optimum thickness exists that depends on Re . At higher Re , the vortical structure differs for each thickness with the deflection angle, whereas at low Re , the location of the separation point strongly influences the hydrodynamics. *Published by AIP Publishing.*

<https://doi.org/10.1063/1.5034439>

I. INTRODUCTION

Undulatory locomotion is widely used by aquatic animals for propulsion. Studies on this type of motion, which have attracted considerable attention,^{1–3} are motivated by not only the desire to understand the mechanism through which fish swim but also the application of undulatory foils for the propulsion of autonomous underwater vehicles (AUVs) and for power generation.

Aquatic animals swim in a wide range of Reynolds numbers (Re) and exhibit various ranges of body shapes. For example, in the complete life cycle of zebrafish from larvae to adult, Re can range from 10 to 10^5 , and the body shape and size vary greatly among the different stages.^{4,5} At different Re values, swimmers employ different propulsion mechanisms. Viscous forces dominate the swimming for small, slow swimmers, whereas inertial forces dominate the flow for large, fast swimmers.⁶ The effect of the shape on the swimming performance in different regimes also differs.⁷

In recent years, substantial attention has been focused on the swimming performance and wake type for a small range of Re values.^{8–11} Relatively few studies have systematically investigated the effects of Re on the swimming performance. For example, Borazjani¹² investigated the effect of Re on the carangiform swimming performance. Simulations were performed for Re values of 300, 4000, and infinity, following which they defined a critical Strouhal number at which the thrust equals the drag; they further discovered that this Strouhal number decreases with increasing Re . The swimming efficiency is therefore an increasing function of Re .

The carangiform mode is very inefficient at low Re , while a higher propulsive efficiency can be achieved only at an infinite Re . Their work was the first in which the effects of Re on the propulsive efficiency were clearly demonstrated. However, they did not use the self-propelled model, which is closer to the characteristics of real aquatic animals, and their study did not take shape effects into consideration. Ashraf investigated the effect of Re on the propulsive performance using a rigid pitching and plunging airfoil.¹³ They consequently revealed the underlying physics behind the changes in the propulsive performance at different values of Re . For relatively low and high Re , the mechanism for optimum performance differs due to variations in the thickness. At lower Re , thin airfoils outperform thick airfoils; at higher Re , thick foils with low pitch amplitudes can achieve significantly better performance.

By contrast, investigations of the shape effect have received little attention. The effect of the chord-thickness ratio on the hydrodynamics of a self-propelled foil was investigated by Zhang,¹⁴ who observed that the chord-thickness ratio can affect the arrangement of vortices in the wake, the symmetry-breaking bifurcation, and the foil velocity. Compared with rectangular foils, it was easy to achieve the optimized Strouhal number for elliptical foils with smaller chord-thickness ratios. Furthermore, the link between a particular shape and the corresponding hydrodynamic constraints was explored by searching for the optimal design for undulatory animals using an evolutionary algorithm.¹⁵ Accordingly, two types of species were obtained that separately exhibited a good efficiency and large stride length. The shape of the efficient swimmers showed a large anterior region separated from the caudal fin by a caudal peduncle with a reduced cross section, whereas the shape of the swimmers with relatively large stride lengths was more elongated than that of the former. Investigations of the effect

^{a)}Author to whom correspondence should be addressed: panguang@nwpu.edu.cn

of the shape on the swimming performance can also be found in Refs. 16–18, but the Re values in those studies were fixed within a small range.

In this paper, we systematically investigate the effects of Re and the thickness of a self-propelled undulatory foil on the propulsive performance. A series of National Advisory Committee for Aeronautics (NACA) airfoils with five thickness sections between 0.04 and 0.24 were employed as the fish model. A large range of Re (50, 500, 1000, 5000, 10^4 , 5×10^4 , 10^5 , and 2×10^5) encompassed the viscous regime, intermediate regime, and inertial regime flows. An immersed boundary method was used to solve the moving boundary problem. Accordingly, the link between the hydrodynamic performance and the flow pattern was established. This study presents specific velocity, force, kinetic energy, power, and efficiency data to help provide a better understanding of propulsive mechanics under different Re values and body shapes.

II. MODEL PROBLEM

A. Kinematics

Functional design has been discussed for every type of fish swimming mode.¹⁹ In this work, we employed one type of body and caudal fin (BCF) swimming mode. The expression of the midline lateral displacement in a local coordinate system has been described in Ref. 20:

$$y(x, t) = A_{max} \frac{x + 0.03125}{1.03125} \sin[2\pi(x - t/T)] (0 \leq x \leq 1), \quad (1)$$

where x is the projected value of the midline on the x -axis, y is the lateral displacement of the midline, A_{max} is the maximum amplitude, and T is the time period, which can be expressed as the reciprocal of the frequency (f). Figure 1 shows the midline of the fish for different instances of one tailbeat cycle with $f = 1/s$ and $A_{max} = 0.125$ m in addition to the amplitude envelope profile. The amplitude envelope reaches a maximum displacement of 0.125 m at the tail of the fish.

B. Nondimensional parameters

Re is defined as follows:

$$Re = \frac{V_{max}L}{\nu}, \quad (2)$$

where $V_{max} = 2\pi A_{max}f$ is the maximum undulatory velocity, L is the length of the fish, and ν is the fluid kinematic viscosity. Throughout this work, the maximum amplitude A_{max} and length L are maintained as constant values of 0.125 m and 1 m, respectively. For a specified value of Re, the kinematic

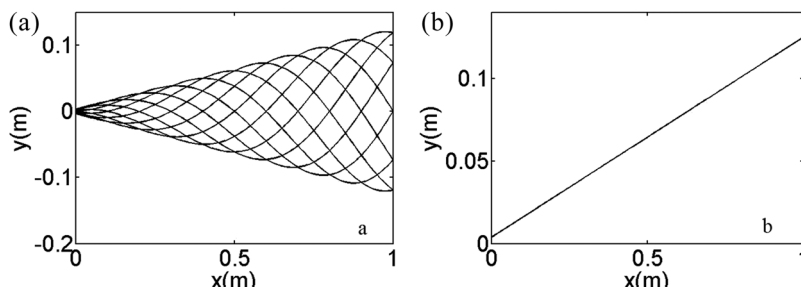


FIG. 1. (a) Midline of the fish for different instances of one tailbeat cycle with $f = 1/s$ and $A_{max} = 0.125$ m and (b) the amplitude envelope profile.

viscosity ν is varied to keep Re constant as the frequency is varied.

The Strouhal number is defined as follows:

$$St = \frac{2A_{max}}{TU_0}, \quad (3)$$

where U_0 is the mean forward velocity of the self-propelled foil.

The definition of the efficiency of the self-propelled problem is controversial.²¹ In some previous studies, the efficiency was defined as the ratio of the thrust power to the input power. However, at the steady swimming state, the thrust force is exactly equal to the drag force, which means the mean net axial force is equal to zero. Thus, this situation introduces difficulties for distinguishing the thrust and drag forces. One approach is based on Lighthill's elongated body theory (EBT), which is expressed as follows:

$$\eta_{EBT} = \frac{1}{2}(1 + U/V), \quad (4)$$

where U is the swimming speed and V is the wave speed of the undulation.²² Although EBT overestimates the efficiency because it neglects the slope of the amplitude function at the tail end, it provides a simple method for calculating the efficiency.¹² In the work of Thiria,²³ the thrust force was measured by fixing the position of the flapping foil using a string attached through a pulley to a calibrated weight and monitoring the weight deficit. In the work of Borazjani,¹² arbitrary decomposition was used to separate the thrust and drag forces,

$$T(t) = \frac{1}{2} \left(\int_A -pn_3 dA + \left| \int_A pn_3 dA \right| \right) + \frac{1}{2} \left(\int_A \tau_{3j} n_{j3} dA + \left| \int_A \tau_{3j} n_j dA \right| \right), \quad (5)$$

$$-D(t) = \frac{1}{2} \left(\int_A -pn_3 dA - \left| \int_A pn_3 dA \right| \right) + \frac{1}{2} \left(\int_A \tau_{3j} n_{j3} dA - \left| \int_A \tau_{3j} n_j dA \right| \right), \quad (6)$$

where $T(t)$ and $D(t)$ are the instantaneous thrust and drag, respectively, n_i is the i -th component of the unit normal vector on dA (the model swims along n_3), τ_{ij} is the viscous stress tensor, and p is the pressure force. In the work of Xiao,²⁴ only the pressure force was considered when computing the thrust power. In this work, we employed the efficiency function proposed by Kern and Koumoutsakos,²⁰ who related the

thrust power to the kinetic energy of the forward motion as follows:

$$\eta = \frac{E}{W}, \quad (7)$$

$$E = \frac{1}{2}mU_0^2, \quad (8)$$

$$m = \rho V_f, \quad (9)$$

$$W = \int_t^{t+T} \oint_S -\sigma \cdot n \cdot U dS dt, \quad (10)$$

where E represents the kinetic energy in the forward direction, W represents the work used by the foil, m is the mass of the foil, the density of the foil ρ is regarded as a constant value equal to the density of the fluid in this work, V_f is the volume of the foil, σ is the viscous stress tensor, n is the outward surface normal vector, U is the velocity of the body surface, and S is the surface of the foil.

Because the mean forward velocity U_0 is a dependent parameter in self-propelled swimming, we set a reference velocity $U_{Ref} = 1$ L/s to nondimensionalize the above parameters. The forward force F_x and lateral force F_y were nondimensionalized by $\rho U_{Ref}^2 L^2$, and the work W and kinetic energy E were nondimensionalized by $\rho U_{Ref}^2 L^3$.

C. Solver

The unsteady flow field around the undulatory self-propelled foil was simulated using a mathematical framework combined with an immersed boundary (IB) method and the adaptive mesh refinement (AMR) technology developed by Bhalla.²⁵ This framework has been described in detail in Ref. 25; thus, only a brief introduction to this method is provided here. This technique employs a conventional IB approach²⁶ with a Cartesian grid. The undulatory body is imposed using a formulation based on Lagrange multipliers. To capture the boundary layers at the body interface and reduce the computational costs, the fluid domain is discretized by a hierarchy of nested grid levels. Each level of the grid is composed of one or more rectangular Cartesian grid patches.

In our work, we employed a four-level Cartesian grid, and the grid spacing ratio between level n-1 and level n is 4.

D. Validation

To validate the above approach, a 2D eel-shaped model is employed in this section. The description of the body width is given as follows:

$$w(x) = \begin{cases} \sqrt{2W_H x - x^2} & (0 \leq x < x_H) \\ W_H \frac{L-x}{L-x_H} & (x_H \leq x < L) \end{cases}, \quad (11)$$

where $W_H = x_H = 0.04$ L and the length of the model L is 1 m. The kinematic motion follows Eq. (1) with $A_{max} = 0.125$ m and $T = 1$ s. ν is selected as 1.4×10^{-4} m²/s, which is related to $Re = 5609$.

In our work, we employed a dynamic time step that satisfies a maximum Courant-Friedrichs-Lowy (CFL) number ≤ 0.1 .

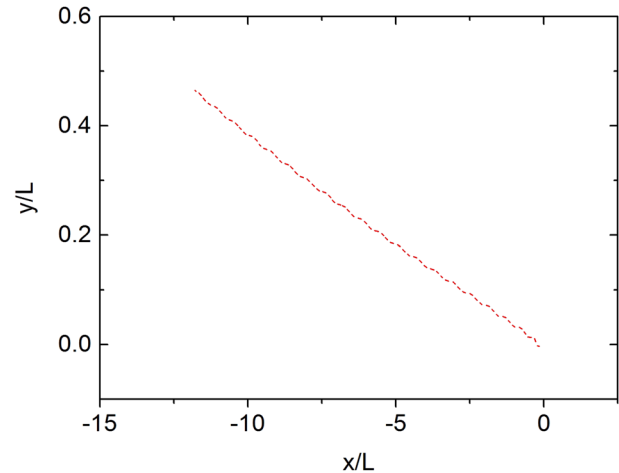


FIG. 2. The trajectory of the center of mass of the model.

A convergence study was conducted in a 10 L \times 4 L periodic domain with four different grids consisting of 20×8 , 30×12 , 40×16 , and 50×20 grid cells in the coarsest-level patch equivalent to 1280×512 , 1920×768 , 2560×1024 , and 3200×1280 grid cells, respectively, in the domain. The relative differences in the mean swimming velocity of the model between the two grid refinements are 7.28%, 3.19%, and 0.41%, respectively. We chose the grid with 40×16 grid cells in the coarsest-level patch for the following simulations.

Figure 2 shows the trajectory of the center of mass of the model, and the forward and lateral velocities are shown in Fig. 3. As shown in these figures, the model accelerates from rest to an asymptotic mean forward velocity of 0.61 L/s in approximately 7 periods. The mean lateral velocity is approximately 0.02 L/s. There are two cycles of oscillation in the forward velocity and one cycle in the lateral velocity for one cycle of body movement. The amplitudes of the oscillations in the forward velocity and lateral velocity are 10% and 9%, respectively, of the asymptotic mean forward velocity. As shown in Fig. 2, the trajectory of the model is not precisely located along the midline of the domain; this is because asymmetric starting maneuvers produce an

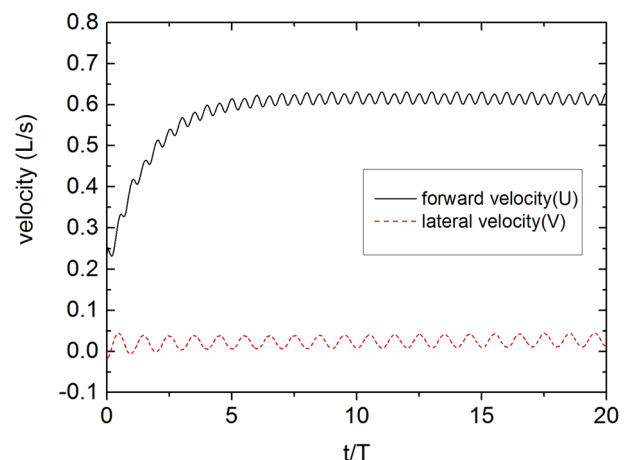


FIG. 3. Temporal evolution of the forward and lateral velocities.

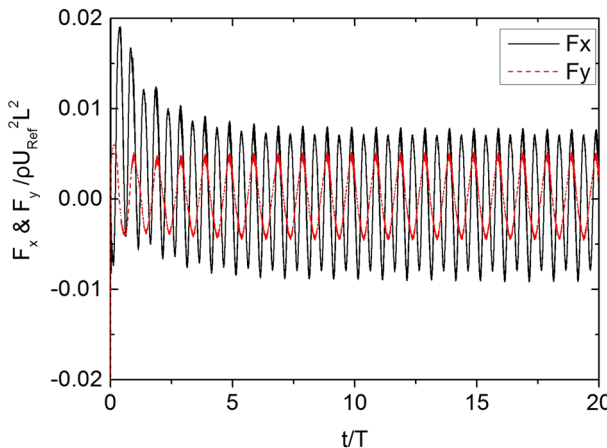


FIG. 4. Temporal evolution of the longitudinal and lateral forces.

asymmetric force.²⁷ The longitudinal force and lateral force during the movement cycles are plotted in Fig. 4. These forces converge to an oscillation mode with a near-zero mean value, and the amplitude of the longitudinal force is approximately 1.5 times the lateral force. When the maximum longitudinal force is reached, the model simultaneously experiences a significant lateral force.

A comparison of the mean velocities U_0 and V_0 and the amplitude values ΔU_0 and ΔV_0 with the results in the literature is presented in Table I. The results of this study show good agreement with the previous results.

To date, IB methods have been applied to problems with high Re values with good success.^{28,29} By using the AMR technology, a comparable spatial resolution can be achieved with relative ease, especially in regions with a large gradient. This approach can avoid a simultaneous grid refinement in all coordinate directions, which would significantly increase the cost of computation. Using the same adaptive IB solver as employed in the present work, Tytell²⁹ simulated the fluid motion around a lamprey model, and the swimmer achieved an Re value on the order of 10^4 with three levels of grid refinement. The agreement with the data from living fishes suggests that computations of undulatory swimming at high Re values can be successfully performed using IB methods. To ensure that the mesh algorithm did not affect the computational results at high Re, a convergence study was also performed at $Re = 2 \times 10^5$. The relative difference in the mean swimming velocity between the 40×16 and 50×20 grid cases was 0.80%. This result means that our grid resolution is sufficiently high for the computation at our test Re. A flow simulation around a captive NACA 0012 airfoil at an attack angle of 0° was performed at $Re = 5 \times 10^5$ to validate the approach for high-Re

TABLE I. A comparison with the results in the literature.

	U_0 (L/s)	ΔU_0 (L/s)	V_0 (L/s)	ΔV_0 (L/s)
Present	0.61	0.016	0.02	0.019
Bhalla ²⁵	0.61	0.019	0.02	0.02
Carling ²⁷	0.60	0.054	0	0.06
Kern ²⁰	0.54	0.02	0	0.04

TABLE II. Drag coefficients for the flow around a captive NACA 0012 airfoil.

	Re	C_d
Present	5×10^5	0.0113
Experiment ³¹	6.6×10^5	0.0111
Shock ³⁰	5×10^5	0.0120

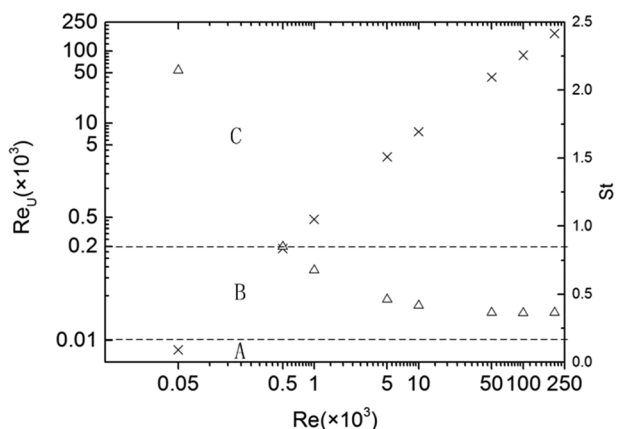
flow. The result was compared with the available experimental data for a similar Re and with the numerical results reported by Shock,³⁰ as shown in Table II. Although the present method is limited by its low-order accuracy due to its use of regularized delta functions and a time step splitting approach,²⁵ the drag coefficient is not very different from the results in the literature.

III. RESULTS AND DISCUSSION

A. Effect of the Reynolds number

In this section, eight Re values ($50, 500, 1000, 5000, 10^4, 5 \times 10^4, 10^5$, and 2×10^5) were selected. The 2D symmetric NACA 0012 foil was employed to undertake the undulatory motion. The amplitude was fixed at 0.125 m, and the frequency (f) varied from 0.3/s to 1.3/s with an interval of 0.1/s.

Hydrodynamic regime categorization can provide a useful approximation of the dominant hydrodynamic forces. Weihs³² classified the flow of swimmers into three regimes: the viscous regime ($Re < 10$), in which viscous forces dominate; the inertial regime ($Re > 200$), in which inertial forces dominate; and an intermediate regime (between 10 and 200), in which both types of forces are important. Most larval swimming behavior occurs in the viscous and intermediate regimes, whereas adults swim in the inertial regime.³³ Weihs employed the movement Reynolds number $Re_U = U_0 L / \nu$ to characterize the ratio of the inertial force to the viscous force. Figure 5 shows the Re values in our work versus Re_U ; we found that the flow for $Re = 50$ is in the viscous regime, while the flow for $Re = 500$ is in the intermediate regime, and the remaining flows are within the inertial regime. The vorticity contours clearly illustrate the

FIG. 5. The Reynolds number (Re) of the present study versus the movement Reynolds number Re_U (shown as \times) and the Re versus the Strouhal number St (shown as \triangle). Regions A, B, and C correspond to the viscous regime, intermediate regime, and inertial regime,³² respectively.

differences among the flows in each regime, which will be analyzed subsequently.

1. Propulsive properties

The mean forward velocity U_0 , input work w , propulsive efficiency η , and lateral force F_y with different frequencies for all of the tested Re values are shown in Fig. 6. The mean forward velocity increases almost linearly with increasing frequency, and the increase rate is larger at higher Re. At a fixed frequency, the self-propelled foil can obtain a higher forward velocity at higher Re. The foil tends to perform more work at lower Re, and it achieves a higher propulsive efficiency at higher Re, which was also observed by Liu.³⁴ At low Re, viscous forces dominate the hydrodynamics of the foil. Thus, the viscous forces are larger than those at higher Re. Weihns³² found that the drag coefficient is inversely proportional to the velocity at lower Re; thus, low-speed motion is very costly in terms of the energy expenditure. The work required is significantly higher at $Re = 50$, as shown in Fig. 6(b). Large viscous forces also result in large lateral forces. As shown in Fig. 6(d), the amplitude of the lateral force at $Re = 50$ is larger than that at $Re = 500$ and 1000 . Moreover, the amplitude increases with increasing Re as the inertial force begins to dominate the flow. For a given value of Re, the efficiency varies little with increasing frequency; this indicates that for swimmers, the efficiency is dominated by Re, and fishes with

the same Re always share the same efficiency. This trend is more obvious at lower Re, where the efficiency remains almost constant.

Note that the velocity changes little with Re beyond an $Re \approx 5 \times 10^4$. Moreover, this trend can also be observed in the variations in the work and efficiency, as shown in Figs. 6(b) and 6(c), respectively, indicating that the effect of Re is asymptotic beyond an $Re \approx 5 \times 10^4$. Panton³⁵ showed that the drag coefficients of bluff bodies tend to asymptotically approach a constant value as Re increases, as was also found by McHenry⁵ through dead drag measurements of zebrafish in the inertial regime, which can present a qualitative explanation of the asymptotic Re effect. The changes in the drag are not presented in our work due to the difficulty associated with distinguishing between drag and thrust (stated in part IIB), while the lateral forces in Fig. 6(d) can reflect the asymptotic phenomenon of the lateral force on swimmers. This asymptotic phenomenon can also suggest that larger animals such as sharks, seals, and dolphins swimming at higher Re numbers in BCF mode always exhibit a maximum efficiency regardless of the frequency and that there is an upper limit on the swimming speed and lateral forces.

The results of our work clearly indicate that the swimming velocity and efficiency are increasing functions of Re, which is consistent with the performance of zebrafish in different life stages.⁵ Although the kinematics in BCF mode can

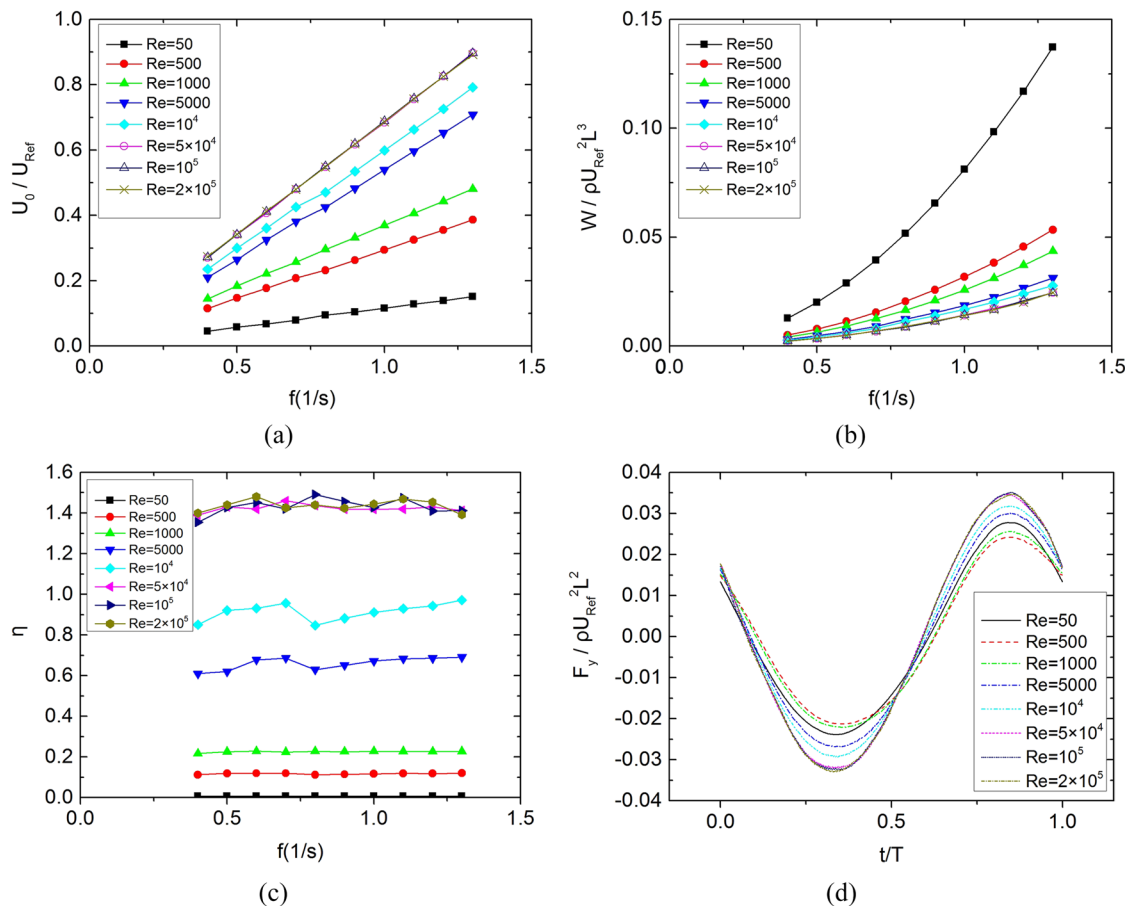


FIG. 6. Variations in the (a) mean forward velocity, (b) work performed by the foil, (c) efficiency with the frequency at different Re value, and (d) lateral force evolution in one period at $f = 1/s$.

achieve self-propulsion for all of our simulated Re values, i.e., the kinematics can produce sufficient thrust to overcome the drag, swimming is very inefficient at low Re. This may represent an explanation for why flapping modes do not occur in animals at very low Re ($Re < 15$).³⁶ In this range of Re values, the rowing mode is more efficient than the flapping mode, and thus, it has been used by a representative group of animals, such as *Bosmina longirostris* and *Speleonectes lucayensis*.^{37,38}

2. 2D wake structure

The vorticity contours at different Re are shown in Fig. 7. Our simulations revealed different wake patterns that strongly depend on Re. In the viscous regime ($Re = 50$), the main characteristic of this wake pattern is that the boundary layer separates from the front of the body, thereby forming the leading-edge vortex that fails to be shed into the downstream region. The failure to shed the boundary layer into the downstream region and the presence of leading-edge vortices create large low-pressure regions that lead to high lateral forces. Therefore, these findings can explain why the lateral forces at $Re = 50$ are larger than the swimmer at $Re = 500$ and 1000, and it also explains the large power expenditure, as ascertained from Figs. 6(b) and 6(d).

In the intermediate regime ($Re = 500$), the foil is enveloped by a boundary layer whose thickness is comparable to its width. The boundary layer separates from the posterior part of the body and sheds into the downstream region to form a thrust-type wake known as a reverse von Kármán vortex street. In this wake, there exist two vortices with opposite signs during one swimming period (i.e., a 2S-type wake). The occurrence of a 2S-type reverse von Kármán vortex street

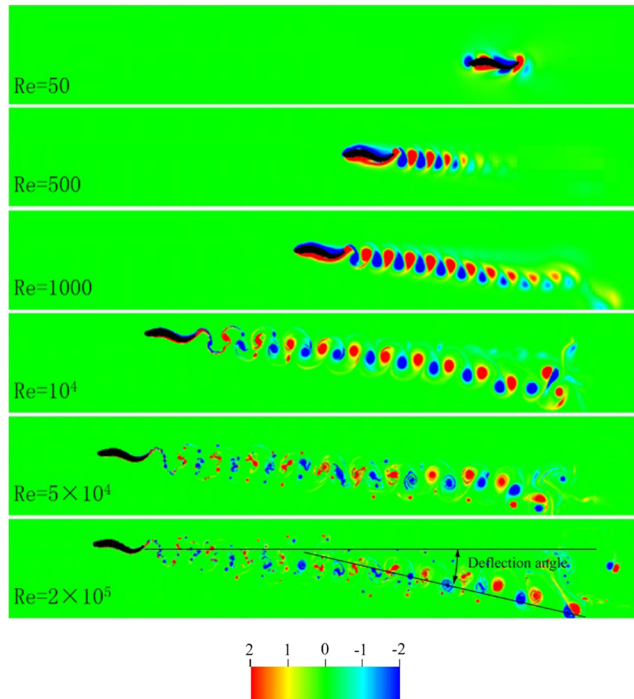


FIG. 7. Vorticity contours with $f = 1/s$ at $t/T = 15$. The vorticity varies between -2 and 2 s^{-1} .

suggests an increase in the thrust force. However, due to the relatively large viscous diffusion effect, the wake dies off rapidly. The backward separated position slightly improves the performance. During the transition to the inertial regime ($Re = 1000$), in which the inertial force begins to dominate the flow, the boundary layer separation point moves toward the trailing edge, and the vortices can spread downstream over a long distance, resulting in increases in the forward velocity and efficiency.

As Re increases to 10^4 , the shear layer becomes considerably thinner. A 2P-type wake forms here, as was shown in the experimental work by Schnipper³⁹ and in the flow patterns of larval fish.⁴ In a 2P-type wake, two vortex pairs exist during one swimming period, and the two vortices in one pair have opposite signs. In the downstream flow, the vortices merge into two large ones and gradually form a von Kármán vortex street in our simulation. The transition from 2S to 2P suggests a significant hydrodynamic promotion. Furthermore, as shown in Fig. 6(a), the velocity and efficiency increase to as high as 62% and 300%, respectively, for Re from 1000 to 10^4 .

As Re increases further, the shear layer becomes unstable and generates a series of eddies between the vortex pairs, which is probably due to the Kelvin-Helmholtz instability.⁴⁰ This type of wake suggests an upper limit effect of Re in addition to the maximum efficiency and lateral forces of the foil. Such vortical structures were also observed by Zhang⁴¹ in a passively flapping flat plate. In our simulations, there is one vortex pair in addition to two single small vortices during one half-period at $Re = 5 \times 10^4$ near the foil. In the downstream wake, the small vortices merge into one large vortex. After an approximately six-period cycle, a von Kármán vortex street forms again. At higher Re , the vortical structure type is similar to this case. However, a greater number of small vortices form.

To investigate the transition in the flapping foil's wake type, Schnipper³⁹ defined a width-based Strouhal number $St_D = \text{thickness } f/u$ and mapped a phase diagram of the vortex type region spanned by St_D and the dimensionless amplitude. In our simulation, the vortex types at $Re = 500, 1000$, and

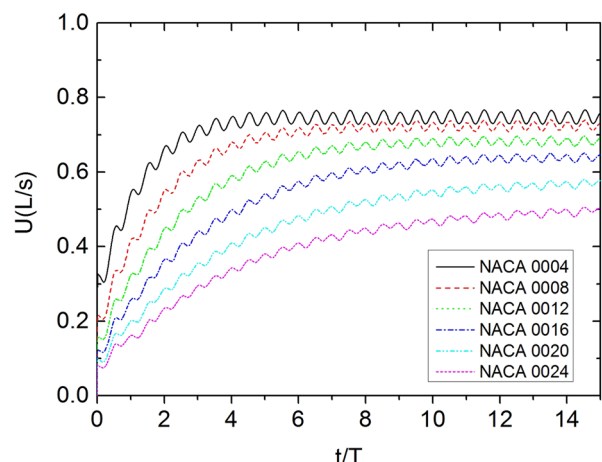


FIG. 8. Temporal evolution of the forward velocity with $f = 1/s$ and $Re = 5 \times 10^4$ at different thicknesses.

5000 are within the range of 0.1~0.3, which is dominated by a 2S-type wake. At $Re = 10^4$, however, St_D is 0.2. This value is beyond the range of 0 ~ 0.1 proposed in their phase diagram for the present 2P-type wake. However, the increase in the total number of vortices at lower St_D values is consistent with the experiment in Ref. 39.

It should be noted that another characteristic of the wake is that although the geometry and the motion of the swimmer are symmetric, the wake becomes deflected such that the positions of the vortex structures are asymmetric about the

swimmer's plane of symmetry. One qualitative explanation for this process is that the self-advection of the dipolar structure is sufficiently strong such that it decouples from the subsequent vortex in the street⁴² with an induced velocity vector inclined toward the downstream direction. Another factor lies in the fact that the undulatory motion of the swimmer produces an effective angle of attack, resulting in a normal force vector that has a component in both the forward direction and the lateral direction. At the start-up stage, the lateral forces are periodic, but the mean net lateral force is non-zero (from Fig. 4).

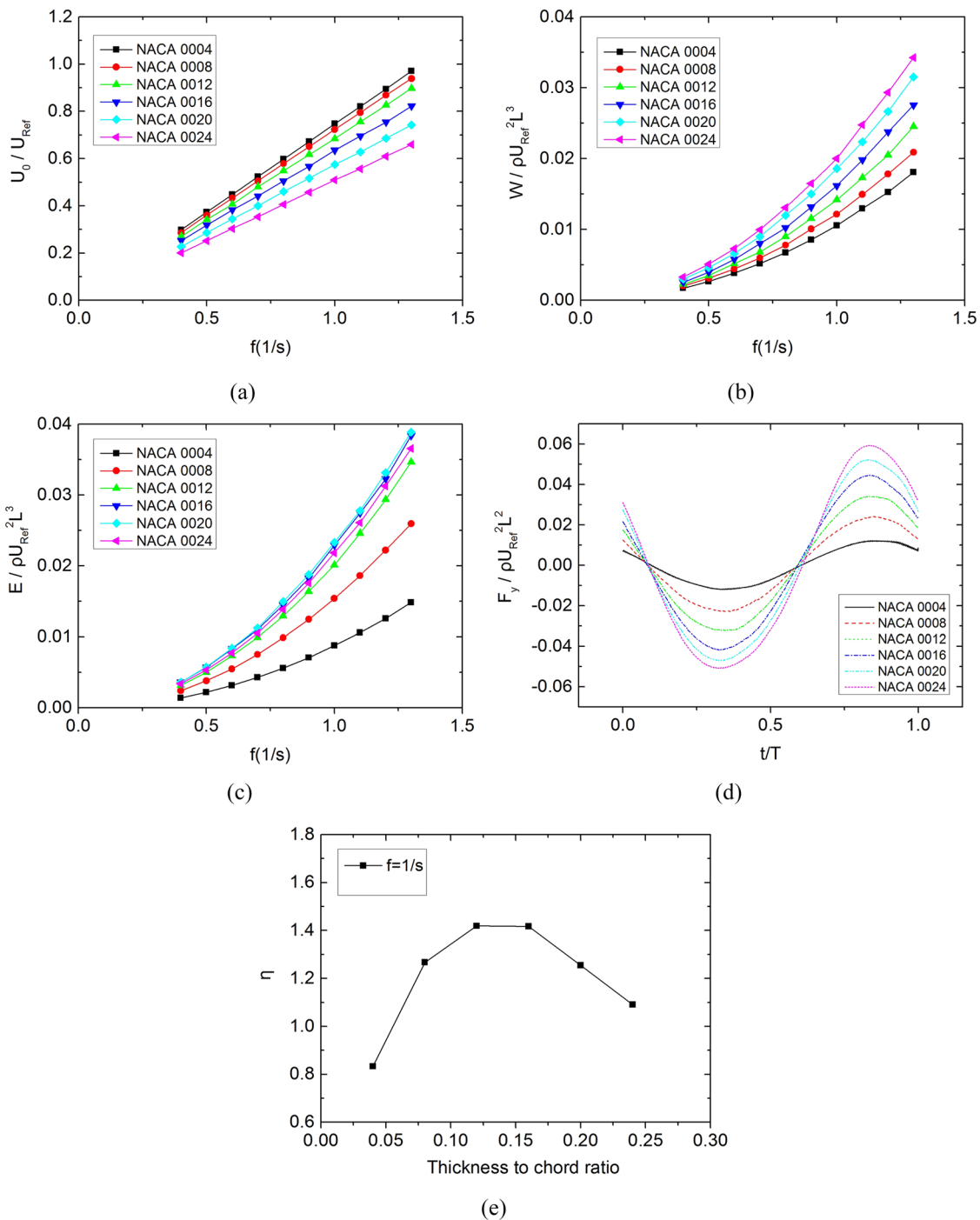


FIG. 9. Variations in the (a) mean forward velocity, (b) work performed by the foil, (c) kinetic energy with the frequency at different thicknesses, (d) lateral force evolution in one period, and (e) efficiency with the thickness at $f = 1/s$ (the efficiency varies little with the frequency, so only the result at one frequency is shown) at $Re = 5 \times 10^4$.

This is because the starting undulation produces an initial trajectory of the center of mass that results in an asymmetric flow. The lateral force produces a lateral velocity, thereby producing a lateral deviation in the vortices. After the start-up stage, the lateral velocity stabilizes and persists in the undulatory period. Jones⁴³ indicated that the direction of the deflection angle is determined by small, initial perturbations. The asymmetric initial flow in our simulations deflects the vortex down the center line. However, while asymmetric vortex streets have been observed in many experiments,^{42–44} to the best of our knowledge, much less attention has been directed toward the effect of Re. As seen in Fig. 7, the deflection angle of the wake increases with increasing Re. This is because the swimmer experiences a larger lateral force, and the dipolar structure is stronger at higher Re, resulting in a larger vortex lateral velocity.

3. Relationship between St and Re

Re and St are the most important nondimensional parameters that characterize the steady performance of swimmers. Experiments have suggested that fishes and even flying animals appear to flap with an optimal Strouhal number near an St of 0.3 for a maximum propulsive efficiency.^{1,45} It was found in Sec. III A that St ranges between 0.3 and 2.1 in our study (as determined from Fig. 5) and increases with decreasing Re. St approaches the aforementioned optimal range only at $Re \geq 10^4$. Some data have shown that fishes may swim with apparently nonoptimal St values during swimming, particularly at lower speeds. For example, Pacific salmon swims at a low speed of 0.5 L/s, which results in an St exceeding 0.6.⁴⁶ Thus, this optimal St value depends on the Re of the flow and is not a constant value.⁴⁶ Lauder and Tytell commented that these fishes may genuinely swim inefficiently at slow speeds or that St alone may not explain the complexities of fish swimming at low Re. The results in our study could offer a possible explanation for Pacific salmon that swims at high St simply because St increases with decreasing Re.

B. Effect of the thickness

In this section, the effect of the thickness on the undulatory self-propelled foil was investigated by using six 2D airfoil sections: NACA 0004, NACA 0008, NACA 0012, NACA 0016, NACA 0020, and NACA 0024. We defined the volume of the 2D foil as the volume per unit depth. Thus, the corresponding volumes V_f of the six foils are 0.03146 m^3 , 0.05887 m^3 , 0.08621 m^3 , 0.1135 m^3 , 0.1408 m^3 , and 0.1681 m^3 . The BCF mode is seldom used by animals in the viscous regime, as stated in Sec III A. Thus, two Re values (5×10^4 and 500) were selected that encompass the inertial regime and the intermediate regime.

1. $Re = 5 \times 10^4$

The temporal evolution of the forward velocity is shown in Fig. 8. The thinner foil can reach a steady movement state faster; because the thinner foil has less mass, it has a smaller inertia. Increasing the thickness increases the form drag; thus, the forward velocity becomes larger with decreasing foil thickness, as shown in Fig. 9(a). With an increasing frequency, the velocity increase is more obvious. We also find that the rate

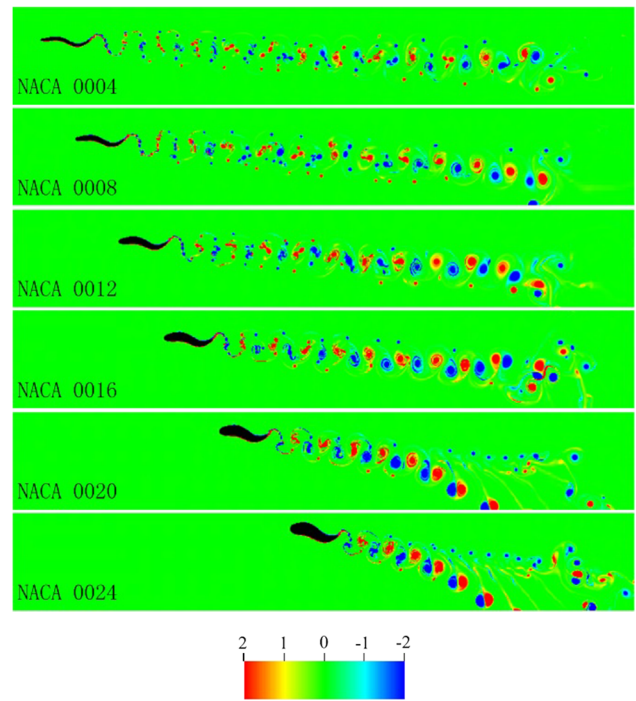


FIG. 10. Vorticity contours with $f = 1/\text{s}$ at $Re = 5 \times 10^4$ and $t/T = 15$. The vorticity varies between -2 and 2 s^{-1} .

of increase of the velocity due to a variation in the thickness is different. As the thickness decreases by 0.04, the increases in the forward velocity are 10.7% and 9.2% at $f = 1.3/\text{s}$ with NACA 0020 and NACA 0012, respectively. However, with NACA 0012 and NACA 0004, the increases are only 4.6% and 3.4% at the same frequency.

The work performed by the foil, the kinetic energy, and the temporal evolution of the lateral force during one period are shown in Figs. 9(b)–(d), respectively. The results imply that additional work is performed by the foil with a larger thickness due to the larger force produced by the thicker foil. Furthermore, the kinetic energy experiences a maximum value at thicknesses of 0.20 and 0.16. In our study, we employed the concept of the efficiency, which is related to the ability

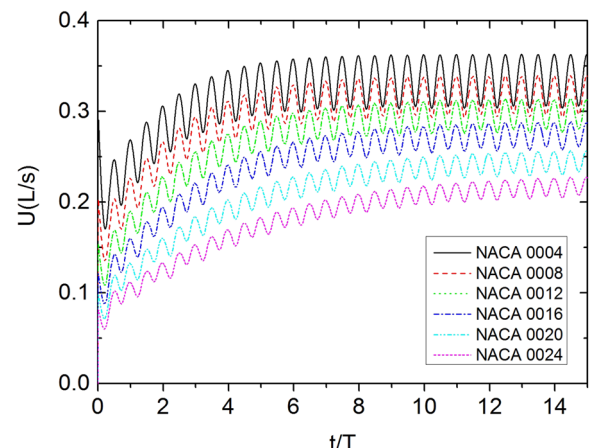


FIG. 11. Temporal evolution of the forward velocity with $f = 1/\text{s}$ and $Re = 500$ at different thicknesses.

to transform the input power into the kinetic energy of forward motion. It should be noted that this definition takes mass into consideration, which is more reasonable for a study of the thickness because the mass varies with changes in the thickness. Although the NACA 0004 foil can achieve the largest forward velocity and spend the least power, i.e., it exhibits the highest swimming economy (defined as the swimming velocity divided by the input power⁴⁷), it has the smallest kinetic energy, and the kinetic energy takes the least proportion of the input power, which results in the lowest efficiency, as shown in

Fig. 9(e). Although NACA 0020 has the largest kinetic energy, it expends the most power; thus, its efficiency is lower than that of NACA 0016. The different sensitivities of the kinetic energy E and input power to the thickness cause the efficiency to initially increase and then decrease with increasing thickness. From the observations of McHenry,⁵ zebrafish have a more elongated shape during their larval stage. Thus, our result can provide an explanation from the perspective of the shape effect insomuch that fish swim more efficiently in the adult stage than in the larvae stage.

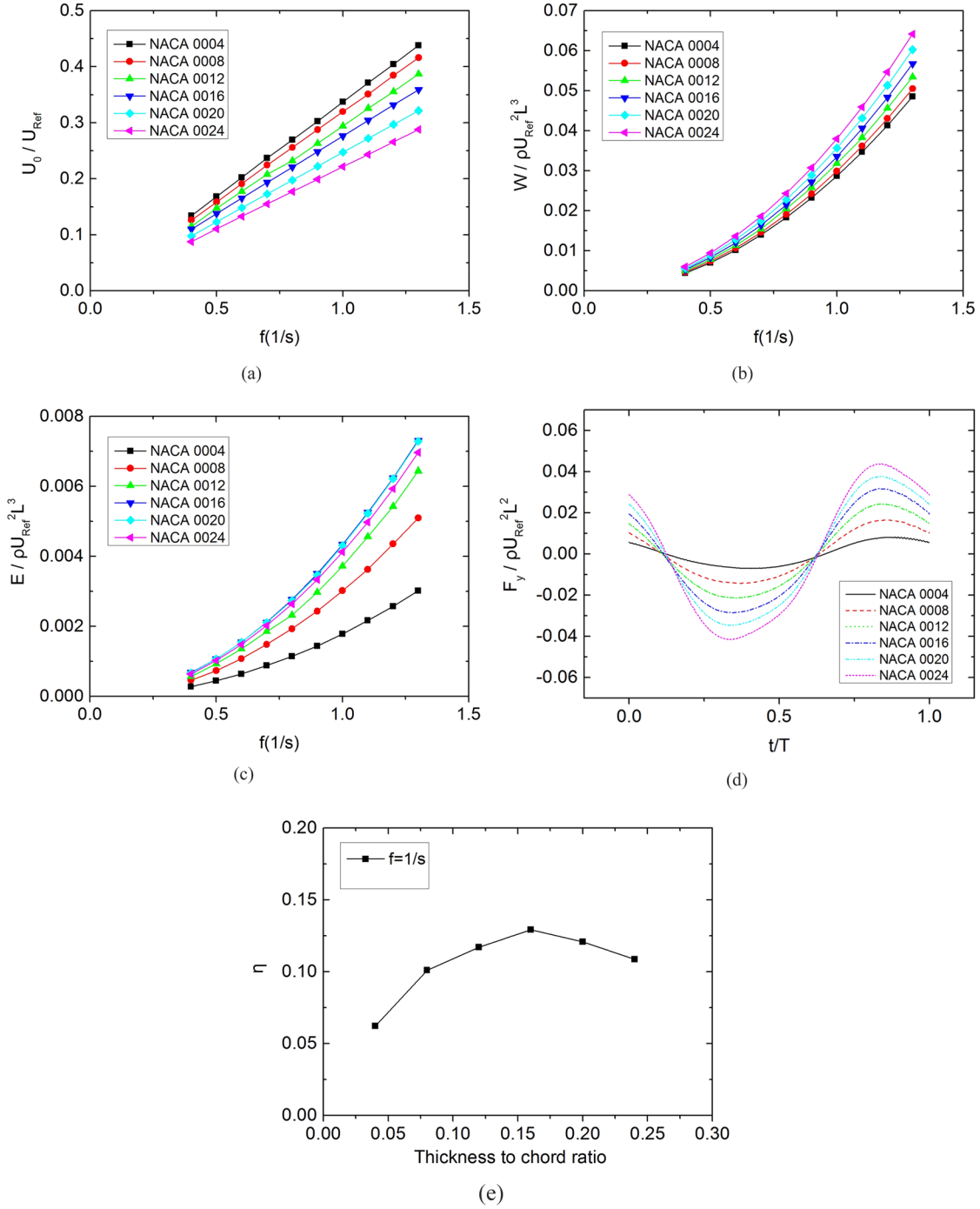


FIG. 12. Variations in the (a) mean forward velocity, (b) work performed by the foil, (c) kinetic energy with the frequency at different thicknesses, (d) lateral force evolution in one period, and (e) efficiency with the thickness at $f = 1/\text{s}$ (the efficiency varies little with the frequency, so only the result of one frequency is shown) at $\text{Re} = 500$.

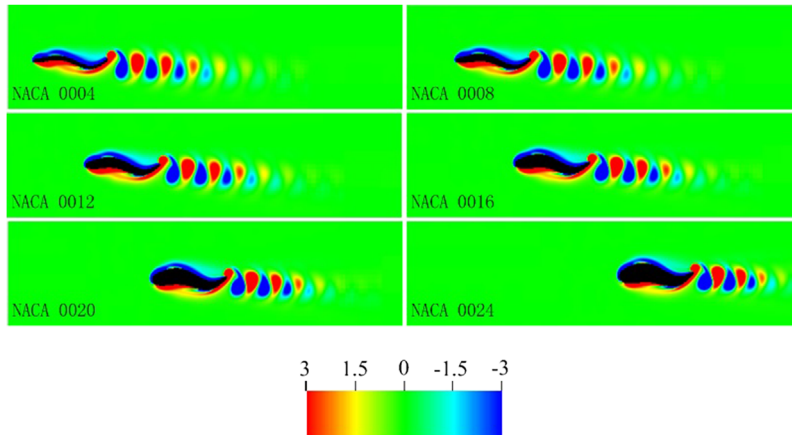


FIG. 13. Vorticity contours with $f = 1/s$ at $Re = 500$ and $t/T = 15$. The vorticity varies between -3 and 3 s^{-1} .

The instantaneous vorticity contours of the six foils with different thicknesses at $f = 1/s$ are presented in Fig. 10. The vortex types in the upstream wake near the foil are similar. Because the small vortices coalesce into large vortices when they evolve, the downstream vortices are stronger than the upstream vortices. We note that with decreasing thickness, a longer period is required for the vortices to coalesce into larger ones. This is due to the greater instability of the thinner foil structures with higher velocities.

We found that the fast formation of the large vortices downstream is associated with a larger input power. We also observed that large vortices propagate to the right obliquely and that larger vortices propagate farther from the center line for thicker foils. As analyzed in the effect of Re , this deflection of the vortex is due to the lateral forces and the formation of the dipolar structure. The pressure distribution difference between the upper and lower surfaces produces a larger lateral force, and the dipolar structure is stronger for thicker foils, thereby generating a vortex street with a larger angle of deflection. As shown in Fig. 10, the inverted von Kármán vortices of NACA 0024 in the downstream wake are seriously deflected downward, and the vortices shed in one period become increasingly closer to one another and have a tendency to coalesce.

2. Re = 500

At $Re = 500$, the thinner foil can also reach a steady movement state in a shorter period, as shown in Fig. 11. However, this superiority is not obvious compared with the motion at higher Re due to larger viscous forces. Moreover, the amplitude of the oscillations in the forward velocity is larger than that at higher Re . The tendencies of the mean forward velocity, work performed by the foil, kinetic energy, and lateral force evolution are similar to those in the high- Re case (Fig. 12). Extreme values of the kinetic energy and efficiency also exist. The amplitude of the lateral force is smaller than that in the high- Re case, which also diminishes the work performed by the foil. Moreover, the sensitivity of the work performed to the thickness decreases at lower Re . As the thickness increases incrementally by 0.04 from NACA 0004 to NACA 0020, the increases in the work performed by the foil are 4.1%, 5.8%, 6.2%, and 6.2%. At $Re = 5 \times 10^4$, the corresponding increases are 15.6%, 17.5%, 12.3%, and 14.4%.

The maximum value of the kinetic energy occurs at the same thickness as the high- Re case, and the NACA 0016 foil can swim most efficiently.

The vortical structures of the foils at lower Re are shown in Fig. 13. The thicker foil swims more slowly, and thus, the vortex has a smaller initial advection velocity; consequently, the distance between the vortices in a snapshot of the vorticity field is shorter than that in the thinner foil. Due to the larger slope from the maximum thickness point to the trailing edge, the separation point of the boundary layer is located farther forward, and the separated flow area is considerably larger. These characteristics result in a decrease in the velocity and an increase in the power for the thicker foil. In the intermediate regime, viscous forces cannot be ignored. The larger drag of the thicker foil due to its larger surface also weakens the increase in the kinetic energy along with the thickness.

IV. CONCLUSION

The effects of Re and thickness on an undulatory self-propelled foil were numerically investigated using the IB method. Re varied from 50 to 2×10^5 , which encompasses the viscous, intermediate, and inertial regimes. The thickness investigation was performed on NACA airfoils with maximum thicknesses of 0.04, 0.08, 0.12, 0.16, 0.20, and 0.24. Our results suggest that changes in the propulsive performance are largely driven by Re and the body shape.

It was also found that the foil can achieve a higher forward velocity, perform less work, and exhibit a higher propulsive efficiency as inertial forces dominate the flow, which is consistent with the evolution of the performance of zebrafish from the larval to the adult stage.⁵ However, the Re effect is asymptotic beyond $Re = 5 \times 10^4$, indicating that larger swimming animals at higher Re are always at a maximum efficiency regardless of the frequency. Our results can also explain why flapping modes are not always employed by animals at very low Re numbers due to their correspondingly low efficiencies.

We observed four types of vortex structures among the three regimes. The main characteristics of the transition from the viscous regime to the intermediate regime are the shedding of vortices into the downstream region and the

backward separated position. The transition from the intermediate regime to the inertial regime is characterized mainly by the long spread of the 2S vortex street. The appearance of the 2P wake and unsteady, small eddies indicated the hydrodynamic promotion and the asymptotic phenomenon of the Re effect, respectively. The formation of dipolar structures and the non-zero mean lateral velocity of the swimmer result in an asymmetric wake. The deflection angle is larger at higher Re, and more input power is simultaneously expended.

From the investigation of the thickness, the thinner foil can achieve a higher velocity and perform less work in both the intermediate regime and the inertial regime, but it swims at a higher cost. Due to the different sensitivities of the kinetic energy and input power to the thickness, an optimum thickness exists. The NACA 0016 foil can present good performance in both regimes. The mechanisms for the performance differences between the two regimes are also different. At higher Re, the faster coalescence of the vortices and the larger deflection angles for thicker foils cause the expenditure of additional power, whereas at lower Re, the differences in the separation point of the boundary layer influence the velocity distribution and power expenditure. Clearly, the shape effect in swimmers is more complicated than a simple ratio; however, to some extent, our study of the thickness can reflect the effect of the shape on the hydrodynamics of swimmers and their ability to convert input power into kinetic energy, which takes the mass into consideration. Our study was proven to be a reasonable method for describing the propulsive efficiency.

A limitation of our work is that we do not take the torque into consideration when calculating the efficiency, although the presented calculation method can reflect the ability to convert input work into kinetic energy. A similar method was also used by Zhu.⁴⁸ Another limitation is that the analysis employed for the mechanisms in different regimes is implemented from the perspective of the velocity, input work, and wake pattern. Meanwhile, we do not distinguish between the viscous and inertial components of the force. This will constitute a subject of our future research.

ACKNOWLEDGMENTS

This work was supported by the National Science Foundation of China (NSFC) under Project Nos. 51479170, 51709229, and 11502210 and by the National Key R & D Plan of China (under Project No. 2016YFC0301300).

¹M. S. Triantafyllou, G. S. Triantafyllou, and D. K. P. Yue, "Hydrodynamics of fishlike swimming," *Ann. Rev. Fluid Mech.* **32**, 33 (2000).

²G. V. Lauder, "Fish locomotion: Recent advances and new directions," *Ann. Rev. Mar. Sci.* **7**, 521 (2015).

³L. M. Chao, Y. H. Cao, and G. Pan, "A review of underwater biomimetic propulsion: Cruise and fast-start," *Fluid Dyn. Res.* **49**, 044501 (2017).

⁴U. K. Müller, J. G. M. V. D. Boogaart, and J. L. V. Leeuwen, "Flow patterns of larval fish: Undulatory swimming in the intermediate flow regime," *J. Exp. Biol.* **211**, 196 (2008).

⁵M. J. McHenry and G. V. Lauder, "The mechanical scaling of coasting in zebrafish (*Danio rerio*)," *J. Exp. Biol.* **208**, 2289 (2005).

⁶J. J. Videler, *Fish Swimming* (Springer Science & Business Media, 2012).

- ⁷U. K. Müller and J. J. Videler, "Inertia as a 'safe harbour': Do fish larvae increase length growth to escape viscous drag?," *Rev. Fish Biol. Fish.* **6**, 353 (1996).
- ⁸D. B. Quinn, G. V. Lauder, and A. J. Smits, "Maximizing the efficiency of a flexible propulsor using experimental optimization," *J. Fluid Mech.* **767**, 430 (2015).
- ⁹S. Alben, C. Witt, T. V. Baker, E. Anderson, and G. V. Lauder, "Dynamics of freely swimming flexible foils," *Phys. Fluids* **24**, 109 (2012).
- ¹⁰P. A. Dewey, B. M. Boschitsch, K. W. Moore, H. A. Stone, and A. J. Smits, "Scaling laws for the thrust production of flexible pitching panels," *J. Fluid Mech.* **732**, 29 (2013).
- ¹¹C. Eloy and L. Schouveiler, "Optimisation of two-dimensional undulatory swimming at high Reynolds number," *Int. J. Non-Linear Mech.* **46**, 568 (2011).
- ¹²I. Borazjani and F. Sotiropoulos, "Numerical investigation of the hydrodynamics of anguilliform swimming in the transitional and inertial flow regimes," *J. Exp. Biol.* **211**, 1541 (2008).
- ¹³M. A. Ashraf, J. Young, and J. C. S. Lai, "Reynolds number, thickness and camber effects on flapping airfoil propulsion," *J. Fluid Struct.* **27**, 145 (2011).
- ¹⁴X. Zhang, S. Ni, S. Wang, and G. He, "Effects of geometric shape on the hydrodynamics of a self-propelled flapping foil," *Phys. Fluids* **21**, 103302 (2009).
- ¹⁵E. Christophe, "On the best design for undulatory swimming," *J. Fluid Mech.* **717**, 48 (2013).
- ¹⁶N. Vandenbergh, S. Childress, and J. Zhang, "On unidirectional flight of a free flapping wing," *Phys. Fluids* **18**, 014102 (2006).
- ¹⁷D. A. Read, F. S. Hover, and M. S. Triantafyllou, "Forces on oscillating foils for propulsion and maneuvering," *J. Fluid Struct.* **17**, 163 (2003).
- ¹⁸S. An, J. Maeng, and C. Han, "Thickness effect on the thrust generation of heaving elliptic airfoils," *J. Aircr.* **46**, 216 (2015).
- ¹⁹R. W. Blake, "Fish functional design and swimming performance," *J. Fish Biol.* **65**, 1193 (2004).
- ²⁰S. Kern and P. Koumoutsakos, "Simulations of optimized anguilliform swimming," *J. Exp. Biol.* **209**, 4841 (2006).
- ²¹W. W. Schultz and P. W. Webb, "Power requirements of swimming: Do new methods resolve old questions?," *Integr. Comp. Biol.* **42**, 1018 (2002).
- ²²M. J. Lighthill, "Large-amplitude elongated-body theory of fish locomotion," *Proc. R. Soc. B* **179**, 125 (1971).
- ²³B. Thiria and R. Godoy-Diana, "How wing compliance drives the efficiency of self-propelled flapping flyers," *Phys. Rev. E* **82**, 015303 (2010).
- ²⁴Q. Xiao, J. Hu, and H. Liu, "Effect of torsional stiffness and inertia on the dynamics of low aspect ratio flapping wings," *Bioinspiration Biomimetics* **9**, 016008 (2014).
- ²⁵A. P. S. Bhalla, R. Bale, B. E. Griffith, and N. A. Patankar, "A unified mathematical framework and an adaptive numerical method for fluid-structure interaction with rigid, deforming, and elastic bodies," *J. Comput. Phys.* **250**, 446 (2013).
- ²⁶C. S. Peskin, "The immersed boundary method," *Acta Numerica* **11**, 479 (2003).
- ²⁷J. Carling, T. L. Williams, and G. Bowtell, "Self-propelled anguilliform swimming: Simultaneous solution of the two-dimensional Navier-Stokes equations and Newton's laws of motion," *J. Exp. Biol.* **201**, 3143 (1998).
- ²⁸M. Bernardini, D. Modesti, and S. Pirozzoli, "On the suitability of the immersed boundary method for the simulation of high-Reynolds-number separated turbulent flows," *Comput. Fluids* **130**, 84 (2016).
- ²⁹E. D. Tytell, C. Y. Hsu, T. L. Williams, A. H. Cohen, and L. J. Fauci, "Interactions between internal forces, body stiffness, and fluid environment in a neuromechanical model of lamprey swimming," *Proc. Natl. Acad. Sci. U. S. A.* **107**, 19832 (2010).
- ³⁰R. A. Shock, S. Mallik, H. Chen, V. Yakhot, and R. Zhang, "Recent results on two-dimensional airfoils using a lattice Boltzmann-based algorithm," *J. Aircr.* **39**, 434 (2002).
- ³¹E. N. Jacobs and A. Sherman, "Airfoil section characteristics as affected by variations of the Reynolds number," *Tech. Rep. Arch. Image Libr.* **8**, 286C290 (1937).
- ³²D. Weihs, "Energetic significance of changes in swimming modes during growth of larval anchovy, *Engraulis mordax*," *Fish. Bull.* **77**, 597 (1980).
- ³³L. A. Fuiman and P. W. Webb, "Ontogeny of routine swimming activity and performance in zebra danios (Teleostei: Cyprinidae)," *Anim. Behav.* **36**, 250 (1988).
- ³⁴H. Liu, R. Wassersug, and K. Kawachi, "A computational fluid dynamics study of tadpole swimming," *J. Exp. Biol.* **199**, 1245 (1996).

- ³⁵R. L. Panton, *Incompressible Flow* (John Wiley & Sons, Inc., New York, 1984).
- ³⁶J. A. Walker, "Functional morphology and virtual models: Physical constraints on the design of oscillating wings, fins, legs, and feet at intermediate Reynolds numbers," *Integr. Comp. Biol.* **42**, 232 (2002).
- ³⁷R. E. Zaret and W. C. Kerfoot, "The shape and swimming technique of *Bosmina longirostris*," *Limnol. Oceanogr.* **25**, 126 (1980).
- ³⁸K. Kohlhage and J. Yager, "An analysis of swimming in remipede crustaceans," *Philos. Trans. R. Soc., B* **346**, 213 (1994).
- ³⁹T. Schnipper, A. Andersen, T. Bohr, and J. H. Walther, "Fluid forces and vortex wakes of a flapping foil," *J. Fluid Mech.* **633**, 411 (2009).
- ⁴⁰T. E. Faber and J. L. Lumley, *Fluid Dynamics for Physicists* (Cambridge University Press, New York, 1995), pp. 1214–1215.
- ⁴¹J. Zhang, N. Liu, and L. U. Xiyun, "Locomotion of a passively flapping flat plate," *J. Fluid Mech.* **659**, 43 (2010).
- ⁴²R. Godoydiana, C. Marais, J. L. Aider, and J. E. Wesfreid, "A model for the symmetry breaking of the reverse Benard-von Karman vortex street produced by a flapping foil," *J. Fluid Mech.* **622**, 23 (2009).
- ⁴³K. D. Jones, C. M. Dohring, and M. F. Platzer, "Experimental and computational investigation of the Knoller-Betz effect," *AIAA J.* **36**, 1240 (1998).
- ⁴⁴K. D. V. Ellenrieder and S. Pothos, "PIV measurements of the asymmetric wake of a two dimensional heaving hydrofoil," *Exp. Fluids* **44**, 733 (2008).
- ⁴⁵M. S. Triantafyllou, G. S. Triantafyllou, and R. Gopalkrishnan, "Wake mechanics for thrust generation in oscillating foils," *Phys. Fluids A* **3**, 2835 (1991).
- ⁴⁶G. V. Lauder and E. D. Tytell, "Hydrodynamics of undulatory propulsion," *Fish Physiol.* **23**, 425 (2005).
- ⁴⁷D. B. Quinn, G. V. Lauder, and A. J. Smits, "Flexible propulsors in ground effect," *Bioinspiration Biomimetics* **9**, 036008 (2014).
- ⁴⁸X. Zhu, G. He, and X. Zhang, "Numerical study on hydrodynamic effect of flexibility in a self-propelled plunging foil," *Comput. Fluids* **97**, 1 (2014).